



HAL
open science

On the origin of the sharp, low-field pinning force peaks in MgB₂ superconductors

Michael Rudolf Koblishka, Alex Wiederhold, Anjela Koblishka-Veneva,
Crosby S Chang, Kévin Berger, Quentin Nouailhetas, Bruno Douine, Masato
Murakami

► **To cite this version:**

Michael Rudolf Koblishka, Alex Wiederhold, Anjela Koblishka-Veneva, Crosby S Chang, Kévin Berger, et al.. On the origin of the sharp, low-field pinning force peaks in MgB₂ superconductors. AIP Advances, 2020, 10 (1), pp.015035. 10.1063/1.5133765 . hal-02470287

HAL Id: hal-02470287

<https://hal.univ-lorraine.fr/hal-02470287v1>

Submitted on 7 Feb 2020



HAL is a multi-disciplinary open access archive for the deposit and dissemination of scientific research documents, whether they are published or not. The documents may come from teaching and research institutions in France or abroad, or from public or private research centers.

L'archive ouverte pluridisciplinaire **HAL**, est destinée au dépôt et à la diffusion de documents scientifiques de niveau recherche, publiés ou non, émanant des établissements d'enseignement et de recherche français ou étrangers, des laboratoires publics ou privés.

On the origin of the sharp, low-field pinning force peaks in MgB₂ superconductors

Cite as: AIP Advances **10**, 015035 (2020); <https://doi.org/10.1063/1.5133765>

Submitted: 26 October 2019 . Accepted: 14 December 2019 . Published Online: 16 January 2020

Michael R. Koblischka , Alex Wiederhold, Anjela Koblischka-Veneva, Crosby Chang, Kévin Berger , Quentin Nouailhetas , Bruno Douine, and Masato Murakami



View Online



Export Citation

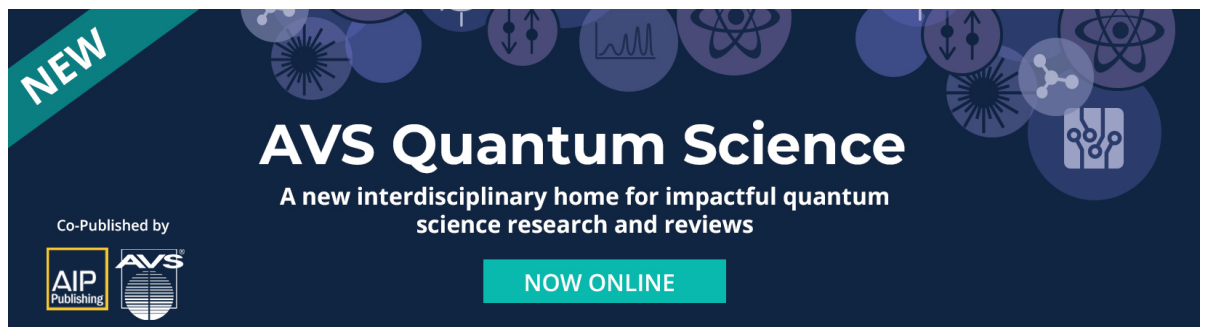


CrossMark

ARTICLES YOU MAY BE INTERESTED IN

[Atomic structures and nanoscale electronic states on the surface of MgB₂ superconductor observed by scanning tunneling microscopy and spectroscopy](#)

Low Temperature Physics **45**, 1209 (2019); <https://doi.org/10.1063/10.0000132>





NEW

AVS Quantum Science

A new interdisciplinary home for impactful quantum science research and reviews

Co-Published by



NOW ONLINE

On the origin of the sharp, low-field pinning force peaks in MgB₂ superconductors

Cite as: AIP Advances 10, 015035 (2020); doi: 10.1063/1.5133765

Submitted: 26 October 2019 • Accepted: 14 December 2019 •

Published Online: 16 January 2020



Michael R. Koblishka,^{1,2,a)} Alex Wiederhold,¹ Anjela Koblishka-Veneva,^{1,2} Crosby Chang,³ Kévin Berger,⁴ Quentin Nouailhetas,^{1,4} Bruno Douine,⁴ and Masato Murakami²

AFFILIATIONS

¹Institute of Experimental Physics, Saarland University, Campus C 6 3, 66123 Saarbrücken, Germany

²Superconducting Materials Laboratory, Department of Materials Science and Engineering, Shibaura Institute of Technology, 3-7-5 Toyosu, Koto-ku, Tokyo 135-8548, Japan

³Institut Jean Lamour, UMR CNRS-Université de Lorraine, 54506 Vandœuvre-lès-Nancy, France

⁴Groupe de Recherche en Energie Electrique de Nancy (GREEN), Université de Lorraine, 54506 Vandœuvre-lès-Nancy, France

^{a)} Author to whom correspondence should be addressed: m.koblishka@gmail.com and miko@shibaura-it.ac.jp

ABSTRACT

Various MgB₂ thin films and single crystals were found in the literature to exhibit a sharp, narrow peak at low fields in the volume pinning force, $F_p(H)$ -diagrams. The origin of this peak is associated with a steep drop of the current density when applying external magnetic fields and is ascribed to sample purity. We show here that bulk MgB₂ prepared by spark-plasma sintering also shows the sharp, narrow peak in F_p . The peak is also seen in the volume pinning force scaling, $F_p/F_{p,\max}$ vs $h = H/H_{\text{irr}}$. Furthermore, polycrystalline bulk MgB₂ samples prepared close to the optimum reaction temperature reveal this peak effect as well, but other samples of the series show a regular scaling behavior. The combination of magnetization data with data from electric transport measurements on the same samples demonstrates the origin of this peak effect. On increasing preparation temperature, the pinning force scaling changes from grain boundary pinning to point pinning and the grain connectivity gets worse. Hence, the sharp, low-field peak in F_p vanishes. Therefore, the occurrence of the peak effect in F_p gives important information on the grain coupling in the MgB₂ samples.

© 2020 Author(s). All article content, except where otherwise noted, is licensed under a Creative Commons Attribution (CC BY) license (<http://creativecommons.org/licenses/by/4.0/>). <https://doi.org/10.1063/1.5133765>

I. INTRODUCTION

The metallic superconductor with the highest transition temperature, MgB₂, is considered as a candidate material for many applications such as trapped field magnets, tapes, and wires due to its simplicity and the simple preparation route possible, even though its T_c is much lower than most of the high- T_c superconductors.^{1,2} Even in sintered, polycrystalline MgB₂ samples, it was found to be possible to establish a current flow through the entire sample perimeter as the grain boundaries (GBs) do not act as weak links, but as flux pinning sites, e.g., in Nb₃Sn.^{3,4} Together with modern cryocooling techniques, the lower T_c does not pose a serious problem.⁵ On the other hand, MgB₂ has its own characteristic magnetic behavior including dendrite-like flux penetration,⁶ flux jump effects,⁷ and peculiar flux pinning properties,⁸ which may influence

possible applications. Therefore, these points must be understood properly.

For the flux pinning behavior, the analysis of the flux pinning forces $F_p = j_c \times B$ (where j_c denotes the critical current density, and $B = \mu_0 H$) using the scaling approach by Dew-Hughes (DH)⁹ and Kramer¹⁰ is an important issue. The flux pinning in MgB₂ is mainly provided by GB-pinning and point-pinning. Two peculiar observations of the flux pinning analysis on MgB₂ include (i) the change of the main acting pinning mechanism with increasing temperature found in polycrystalline samples prepared with varying reaction temperatures¹¹ and (ii) the appearance of a sharp, narrow peak in the $F_p - H$ diagrams at relatively low applied fields.¹²⁻²¹ Such a peak was observed first in MgB₂ single crystals^{22,23} and then in thin films.²⁴⁻²⁶ The occurrence of this peak at relatively low fields was ascribed to the strong decrease in $j_c(B)$ due to sample purity.

In this contribution, we analyze magnetization data obtained on a spark-plasma sintered (SPS) MgB_2 sample with a highly dense microstructure²⁷ and compare the results with a series of sintered, polycrystalline bulk MgB_2 samples prepared with varying reaction temperatures.²⁸ On all samples, we have performed electric transport measurements,^{31,32} the behavior of which enable us now to clarify the origin of the peak found in the F_p -diagrams.

II. EXPERIMENTAL PROCEDURE

The MgB_2 sample was prepared by SPS at 1200 °C and a uniaxial pressure of 50 MPa. The sample reached a density of 2.61 g/cm³ (99.2%).²⁷ Our data are compared to sintered, polycrystalline MgB_2 samples fabricated in the solid state reaction in a pure Ar atmosphere with reaction temperatures between 750 °C and 950 °C.²⁸ For superconducting quantum interference device (SQUID) measurements, small samples (2 mm × 2 mm × 1.5 mm) were cut from the big pellets. For the resistance measurements, small bars (10 mm × 1 mm × 1 mm) were prepared and the contacts were fixed with silver paint, ensuring a 5 mm distance between the voltage pads. The magnetic characterization measurements were performed using SQUID magnetometry (Quantum Design MPMS3), and the magneto-resistance characteristics were recorded using an Oxford Instruments 8 T Teslatron system. The critical current densities were calculated from the magnetization loops using the extended Bean model for rectangular samples.²⁹ Electron backscatter diffraction (EBSD) and transmission electron microscopy (TEM) were performed on TEM-slices prepared using focused ion-beam milling. Details of these procedures are given in Ref. 30 and the [supplementary material](#).

III. RESULTS AND DISCUSSION

Figures 1(a) and 1(b) present j_c as a function of the applied field, $\mu_0 H_a$ (a), and the volume pinning force, F_p , as a function of the field (b) of the SPS sample at various temperatures. In (b), the definitions of H_{peak} denoting the position of the sharp F_p peak and H_{cross} marking the crossover field after the peak are given. The peak and shoulder shape of the $F_p(H)$ curves is observable up to 30 K. The inset to Fig. 1(a) gives the $j_c(H, T)$ data in a double-log plot. Here, two regions are clearly distinguishable, as indicated by the dashed lines. The flat region at low fields can be considered to be the single-vortex pinning region, whereas the connected sloped region is where weak collective pinning is dominant.^{33–35} The values of the exponent β in $j_c(H) \propto H^{-\beta}$ in the sloped region are around 1.0 at 5–25 K, 1.15 at 30 K, and 1.2 at 35 K, indicating that the decreasing slope of $j_c(H)$ gradually becomes steeper at temperatures above 25 K due to thermal fluctuation effects.^{36,37}

Figure 2(a)–2(d) show the peak region of the F_p vs $\mu_0 H_a$ -diagrams for samples SPS (a), S775 (b), S850 (c), and S950 (d). The signature of the sharp F_p -peak is clearly visible in (a) and (b), whereas only traces are seen in (c), and in (d), the $F_p - H$ behavior is fully regular. The pinning force scaling analysis is based on the approach of DH.⁹ The scaled pinning force data $f = F_p/F_{p,\text{max}}$ vs $h = H_a/H_{\text{irr}}$ can be fitted to the functional dependence given by $f = A \cdot (h)^p \cdot (1 - h)^q$, with A being a numerical parameter, and p and q are describing the actual pinning mechanism. The position of the maximum in the F_p plot, h_0 , is given by $p/(p + q)$. For MgB_2 , the pinning at GBs ($p = 0.5$ and $q = 2$) and the pinning at

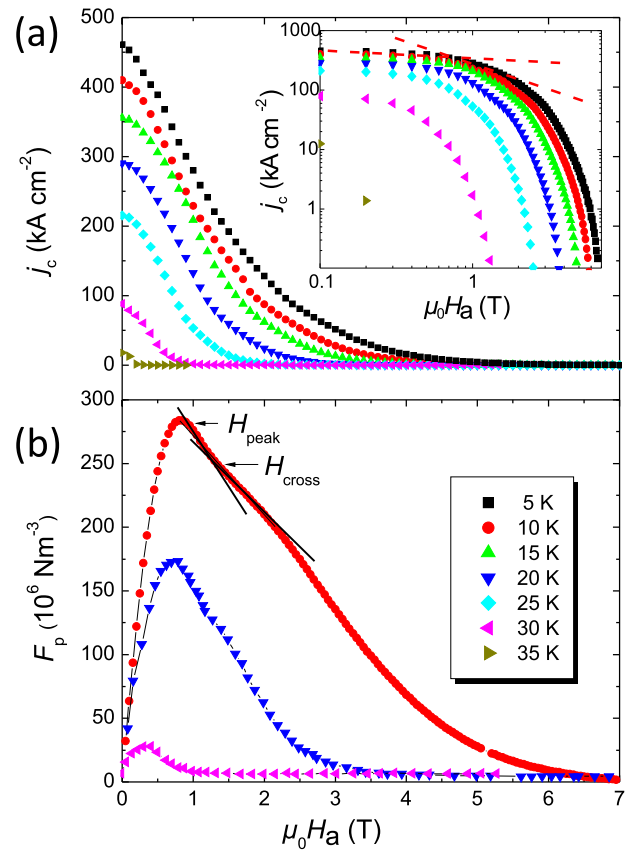


FIG. 1. Data of the MgB_2 SPS sample. (a) j_c as a function of the applied field, $\mu_0 H_{\text{ext}}$, in the temperature range 5 K $\leq T \leq$ 35 K. The inset shows the same data in a double-log plot, together with the linear behavior as indicated by the dashed lines. (b) Pinning force, F_p , as a function of the applied field, $\mu_0 H_{\text{ext}}$, calculated from the $j_c(H_a)$ -data for $T = 10$ K, 20 K, and 30 K. At the 10 K curve, the peak position, H_{peak} , and the crossover field, H_{cross} , are indicated by arrows.

non-superconducting point pins ($p = 1$, $q = 2$) are the most important functions. Figure 2(e) gives the DH-scaling of the SPS sample. The pinning force scaling is well developed, and the fit (red line) to all data yields a peak position $h_0 = 0.21$, which clearly points to a dominant flux pinning provided by extended defects, i.e., GBs. The pinning force scaling of all samples studied is given in Fig. S1 of the [supplementary material](#).

Now, we turn to the origin of the peak effect in the $F_p(H)$ -curves. From the literature, we can extract the following findings concerning the sharp, narrow peak in $F_p(H)$:

- (i) Single-crystals and high-quality thin films exhibit the specific F_p -curve shape.
- (ii) Sintered, polycrystalline samples, normal thin films, and powders do not show any peculiar F_p -curve shape.
- (iii) The peak shows a clear temperature dependence; therefore, matching effects are excluded.
- (iv) The peak is located at relatively high fields, which implies that surface effects are excluded.

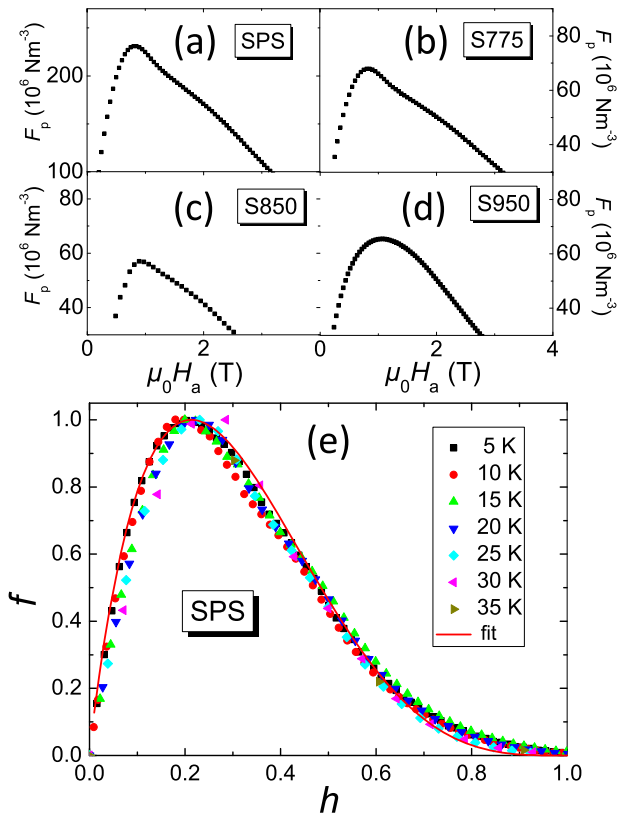


FIG. 2. [(a)–(d)] Pinning forces vs applied field for samples: (a) SPS, (b) S775, (c) S850, and (d) S950. (e) Pinning force scaling, f vs h of the SPS sample.

The peak positions, H_p , and the respective crossover fields, H_{cross} were extracted from the F_p -data. Table I gives the data of all bulk MgB₂ samples and those of Ref. 26 for comparison. The smaller values of Ref. 26 demonstrate the demagnetization effects. The values of H_p are sufficiently large to be above the full penetration field.

TABLE I. Values for H_p and H_{cross} for all MgB₂ bulk samples studied here and those of Ref. 26 (MgB₂ thin film, 700 nm thickness), together with data for $\Delta\rho$ and the connectivity, K . The scaling parameters A , p , and q are found in Table S1 of the supplementary material. All magnetic data are for $T = 10$ K. For details of the electric measurements, see Ref. 32. The * indicates that these values are for the normal peak in F_p , not the sharp peak as in the case of the other samples. Correspondingly, there is no value for H_{cross} . n.a. indicates that there are no data available.

Sample name	H_p (mT)	H_{cross} (mT)	$\Delta\rho$ ($\mu\Omega$ cm)	K (%)
S775	643	907	140	4.51
S800	826	1305	77	8.195
S805	798	1525	37	17.054
S850	802*	...	64	9.859
S950	897*	...	113	5.584
SPS	883	1447	6.5	97.076
Reference 26	54	122	n.a.	n.a.

Figure 3 presents the temperature dependence of the extracted critical fields. H_{peak} and H_{cross} are well below H_{irr} . The values of H_{peak} clearly show a sample size dependence as the values here are much larger as compared to the thin-film data of Ref. 26; thus, demagnetization effects play a role. Here, it should be noted that our values of H_{peak} are outside the range of present-day magneto-optics,^{38,39} and so no direct observations of the flux patterns around H_{peak} are possible.

The first finding of the present work is that sintered, polycrystalline samples prepared at reaction temperatures close to the optimum value (i.e., $\sim 800^\circ\text{C}$ ²⁸) do show the sharp F_p -peak, whereas all other samples prepared at higher T do not. The SPS sample with its high density also exhibits the sharp F_p -peak.

The electric transport measurements elucidate the grain connectivity K , which plays an important role for the current flow through the sample (see Table I). K is calculated from the resistance data obtained via $K = \Delta\rho_g/\Delta\rho$, with $\Delta\rho_g = 6.31 \mu\Omega$ cm for randomly oriented 3D samples, and $\Delta\rho = \rho(300 \text{ K}) - \rho(40 \text{ K})$.⁴⁰ In our series of samples, K was found to increase steeply with increasing reaction temperature from 775 °C to 805 °C and then decreases again when increasing the temperature up to 950 °C (see Fig. S2 of the supplementary material and Ref. 32). The SPS sample shows $K = 0.96$ due to its high density.

Finally, Fig. 4 gives the analysis of the scaled flux pinning curve for one selected sample (S775). To elucidate the acting flux pinning mechanism, one could combine two of the pinning mechanisms of DH and try to fit the data using a linear combination. It is straightforward to assume that the GB pinning is related to the low-field F_p -peak. This is symbolized by the red dashed line (fit 1), obtained using the fitting parameters $p = 1.17$ and $q = 4.98$. The resulting fit is perfect until H_{cross} is reached. Now, we subtract this fit from the experimental data and rescale them with a new H_{max} . The result of this procedure is drawn with a blue line. Finally, these data are again fitted using a DH function with $p = 3.04$ and $q = 1.76$ (fit 2). All this implies that we can fit the experimental data showing the sharp, low-field peak with a combination of two DH pinning

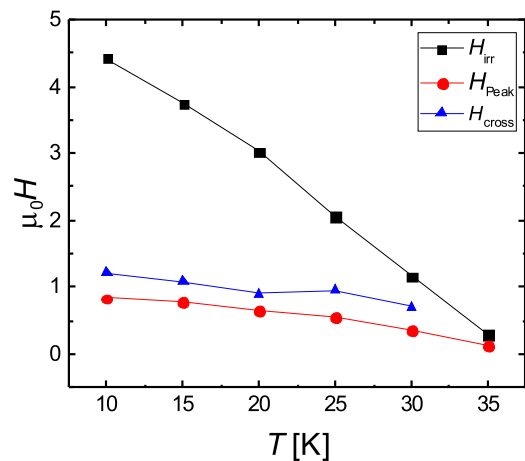


FIG. 3. Irreversibility field, H_{irr} , peak field, H_{peak} , and the crossover field, H_{cross} of sample S775 as a function of temperature. Note that H_{peak} and H_{cross} are considerably smaller than H_{irr} .

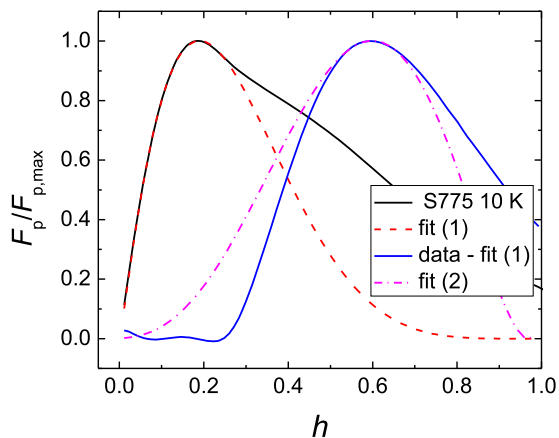


FIG. 4. Pinning force scaling, $F_p/F_{p,\max}$ vs the reduced field, $h = H_a/H_{tr}$ for sample S775 (black line). Fit 1 (red dashed line) attempts to describe the sharp, low-field peak. The blue line indicates the result of subtracting fit 1 from the original data and re-scaling. Fit 2 (dashed-dotted purple line) is then a DH fitting to the blue curve.

functions. The low-field peak in F_p is caused by the GB pinning, whereas the large shoulder is due to pinning at point defects. Together with the information from the electric measurements revealing the grain coupling, we can now come to the conclusion for the origin of the F_p -peak.

As described before, one of the advantages of MgB_2 is the current flow through the entire sample perimeter even in polycrystalline samples. This implies that the currents run across various GBs, affected by the crystallographic orientation of the grains. The first point enables pinning at GBs, which is beneficiary, e.g., in Nb_3Sn . Due to the second point, the currents and flux pinning forces are affected by the given anisotropy of the material.⁴¹ Following the calculations of Eisterer,⁴² the position of the GB pinning peak may be obtained in the range between 0.1 and 0.2, which is, indeed, the case for the sharp, low-field peaks observed here. In this range, the dominating flux pinning is provided by the GBs, and the current flow is affected by the crystal anisotropy and percolation. When a field-induced decoupling occurs, the currents will only cycle in small regions with the minimum size of an individual grain. Then, anisotropy and percolation do not play the important role anymore, and we will have a situation corresponding to polycrystalline $YBa_2Cu_3O_x$. As there is no texture of the MgB_2 grains, the differences in the local currents will average out and we obtain a peak in the F_p diagram for point pinning at $h \approx 0.33$, following a simple DH pinning function with $p = 0.52$ and $q = 0.98$.¹¹

To observe the sharp, narrow F_p -peak, it is essential that the sample is free of additions providing pinning at small, non-superconducting inclusions, as this would strengthen the secondary pinning mechanism. The GB pinning may then only appear as a small shoulder on the low field side, if at all. Furthermore, the sample preparation must ensure that the MgB_2 grains are well coupled (i.e., having a high grain connectivity). Such situation is realized in the SPS sample studied here. Figures 5(a) and 5(b) present TEM images of GBs in this sample, and Fig. 5(c) gives a phase map obtained using electron backscatter diffraction (EBSD). A majority of the GBs

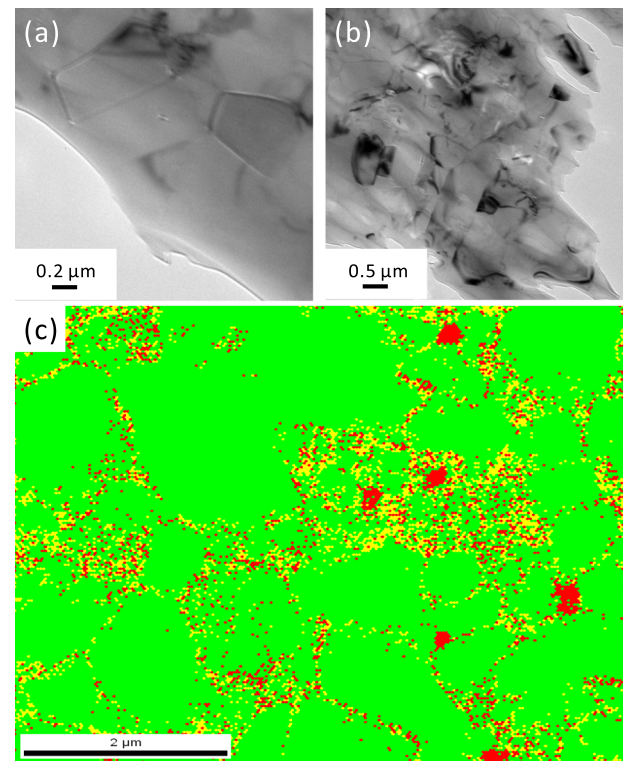


FIG. 5. GBs in the SPS-sample. TEM images of clean GBs (a) and GBs with secondary phase particles (b). (c) presents an EBSD phase map, where green indicates MgB_2 , red MgO , and yellow MgB_4 . More details on their EBSD analysis are found in the [supplementary material](#) and in Ref. 30.

is clean, while others are obscured by MgO and MgB_4 particles, as demonstrated in Ref. 30. The decay of the current flow will then not influence the F_p diagram that much as the peak positions are close to each other. In this sense, the previous explanation that only *pure* samples will exhibit the sharp, narrow F_p -peak is correct.

Table I demonstrates, further, that the peak field, H_{peak} , scales with the sample size when comparing the thin film data with ours. Therefore, this effect will not influence the currently achieved trapped fields in the bulk MgB_2 samples (typical dimensions of 3–5 cm diameter and thickness of 10–20 mm) as the current trapped field values are still relatively low.^{18,43–45} However, when attempting to trap much larger fields, then the change of current flow at H_{peak} will pose a serious problem as one would obtain not one large central trapped field peak, but several smaller ones when the current flow is reduced to smaller islands. This situation would get worse the higher the applied field would be. Hence, H_{peak} is a limiting factor for the maximum achievable trapped field. As the grain connectivity cannot be tuned to be much better (the sharp peaks are seen in single crystals, thin films, and the SPS sample), the only way out is to improve the flux pinning *inside* the MgB_2 grains. Therefore, an ideal MgB_2 sample for applications needs small, nano-sized grains with embedded, strong flux pinning provided by nano-sized pinning centers. In this case, the sharp, low-field peak will be overwhelmed by the flux pinning provided by point-like defects.

IV. CONCLUSIONS

To conclude, we have performed magnetic and electric measurements on a series of sintered, polycrystalline MgB_2 samples. The samples prepared using a low reaction temperature and the high-density, spark-plasma sintered samples exhibit the sharp, low-field peak in F_p , while the other samples do not. The electric transport measurements performed on the same samples reveal a change of the grain connectivity on increasing the preparation temperature, whereas the highly dense, spark-plasma sintered sample shows a well-developed grain connectivity. As a result, from this combination of magnetic and electric measurements, we can conclude that the change of length scale of the current flow at H_{peak} is responsible for the F_p -peak. When the grains are well coupled together, the current flow through the entire sample perimeter is enabled. In this case, the flux pinning is mainly provided by GB pinning, and the crystal anisotropy and percolation play a role. In case the coupling of the MgB_2 grains is worse, we only observe the flux pinning provided by small, non-superconducting inclusions, and the current flow is reduced to grain clusters or grains. This finding may have important consequences for the achievable trapped fields in MgB_2 .

SUPPLEMENTARY MATERIAL

See the [supplementary material](#) for specific information about the pinning force scaling of all samples, the grain connectivity, and experimental details about the EBSD analysis.

ACKNOWLEDGMENTS

We would like to thank J. Noudem (CRISMAT, Caen, France) for the spark-plasma sintered MgB_2 and K. Inoue and M. Muralidhar (SIT, Tokyo, Japan) for the sintered MgB_2 samples. This work is part of the SUPERFOAM international project funded by ANR and DFG under Grant Nos. ANR-17-CE05-0030 and DFG-ANR Ko2323-10, respectively.

REFERENCES

- 1 K. Vinod, R. G. Abhilash Kumar, and U. Syamaprasad, *Supercond. Sci. Technol.* **20**, R1–R13 (2007).
- 2 M. Tomsic, M. Rindfleisch, J. Yue, K. McFadden, J. Phillips, M. D. Sumption, M. Bhatia, S. Bohnenstiehl, and E. W. Collings, “Overview of MgB_2 superconductor applications,” *Int. J. Appl. Ceram. Technol.* **4**, 250–259 (2007).
- 3 D. C. Larbalestier, L. D. Cooley, M. O. Rikel, A. A. Polyanskii, J. Jiang, S. Patnaik, X. Y. Cai, D. M. Feldmann, A. Gurevich, A. A. Squitieri, M. T. Naus, C. B. Eom, E. E. Hellstrom, R. J. Cava, K. A. Regan, N. Rogado, M. A. Hayward, T. He, J. S. Slusky, P. Khalifah, K. Inumaru, and M. Haas, *Nature* **410**, 186–189 (2001).
- 4 M. Eisterer, *Supercond. Sci. Technol.* **20**, R47–R74 (2007).
- 5 R. Radebaugh, *Proc. IEEE* **92**, 1719–1734 (2004).
- 6 T. H. Johansen, M. Baziljevich, D. V. Shantsev, P. E. Goa, Y. M. Galperin, W. N. Kang, H. J. Kim, E. M. Choi, M. S. Kim, and S. I. Lee, *Europhys. Lett.* **59**, 599–605 (2002).
- 7 V. Chabanenkov, R. Puzniak, A. Nabialek, S. Vasiliev, V. Rusakov, L. Huanqian, R. Szymczak, H. Szymczak, J. Jun, J. Karpinski, and V. Finkel, *J. Low Temp. Phys.* **130**, 175–191 (2003).
- 8 Y. Bugoslavsky, G. K. Perkins, X. Qi, L. F. Cohen, and A. D. Caplin, *Nature* **410**, 563–565 (2001).
- 9 D. Dew-Hughes, *Philos. Mag.* **30**, 293–305 (1974).
- 10 E. J. Kramer, *J. Appl. Phys.* **44**, 1360 (1973).
- 11 M. R. Koblischka, A. Wiederhold, M. Muralidhar, K. Inoue, T. Hauet, B. Douine, K. Berger, M. Murakami, and U. Hartmann, *IEEE Trans. Magn.* **50**, 9000504 (2014).
- 12 P. Mikheenko, E. Martinez, A. Bevan, J. S. Abell, and J. MacManus-Driscoll, *Supercond. Sci. Technol.* **20**, S264–S270 (2007).
- 13 E. Martinez, M. Martinez-Lopez, A. Millan, P. Mikheenko, A. Bevan, and J. S. Abell, *IEEE Trans. Appl. Supercond.* **17**, 2738–2741 (2007).
- 14 E. Martinez, P. Mikheenko, M. Martinez-Lopez, A. Millan, A. Bevan, and J. S. Abell, *Phys. Rev. B* **75**, 134515 (2007).
- 15 S. X. Dou, S. Soltanian, J. Horvat, X. L. Wang, S. H. Zhou, M. Ionescu, H. K. Liu, P. Munroe, and M. Tomsic, *Appl. Phys. Lett.* **81**, 3419–3421 (2002).
- 16 A. Yamamoto, J. Shimoyama, S. Ueda, Y. Katsura, S. Horii, and K. Kishio, *Supercond. Sci. Technol.* **18**, 116–121 (2005).
- 17 G. Giunchi, G. Ripamonti, T. Cavallin, and E. Bassani, *Cryogenics* **46**, 237–242 (2006).
- 18 J. H. Durrell, C. E. J. Dancer, A. Dennis, Y. Shi, Z. Xu, A. M. Campbell, N. Hari Babu, R. I. Todd, C. R. M. Grovenor, and D. A. Cardwell, *Supercond. Sci. Technol.* **25**, 112002 (2012).
- 19 T. Naito, T. Sasaki, and H. Fujishiro, *Supercond. Sci. Technol.* **25**, 095012 (2012).
- 20 V. Sandu, *Mod. Phys. Lett. B* **26**, 1230007 (2012).
- 21 P. Badica, G. Aldica, A. M. Ionescu, M. Burdusel, and D. Batalu, in *Correlated Functional Oxides: Nanocomposites and Heterostructures*, edited by H. Nishikawa, N. Iwata, T. Endo, Y. Takamura, G. H. Lee, and P. Mele (Springer, 2017), p. 75.
- 22 Z. X. Shi, A. K. Pradhan, M. Tokunaga, K. Yamazaki, T. Tamegai, Y. Takano, K. Togano, H. Kito, and H. Ihara, *Phys. Rev. B* **68**, 104514 (2003).
- 23 Z. X. Shi, A. K. Pradhan, M. Tokunaga, K. Yamazaki, T. Tamegai, Y. Takano, K. Togano, H. Kito, and H. Ihara, *Physica C* **378–381**, 550–553 (2002).
- 24 S. G. Jung, W. K. Seong, N. H. Lee, and W. N. Kang, *Physica C* **471**, 798–800 (2011).
- 25 S. G. Jung, N. H. Lee, W. K. Seong, K. H. Cho, W. N. Kang, and S. Oh, *Supercond. Sci. Technol.* **24**, 075003 (2011).
- 26 S. G. Jung, W. K. Seong, and W. N. Kang, *J. Phys. Soc. Jpn.* **82**, 114712 (2013).
- 27 J. G. Noudem, L. Dupont, L. Gozzelino, and P. Bernstein, *Mater. Today: Proc.* **3**, 545–549 (2016).
- 28 M. Muralidhar, K. Nozaki, H. Kobayashi, X. L. Zeng, A. Koblischka-Veneva, M. R. Koblischka, K. Inoue, and M. Murakami, *J. Alloys Compd.* **649**, 833–842 (2015).
- 29 H. P. Wiesinger, F. M. Sauerzopf, and H. W. Weber, *Physica C* **203**, 121–128 (1992).
- 30 A. Koblischka-Veneva, M. R. Koblischka, J. Schmauch, J. Noudem, and M. Murakami, *J. Microsc.* **274**, 123–131 (2019).
- 31 M. Jirsa, M. Rames, M. R. Koblischka, A. Koblischka-Veneva, K. Berger, and K. Douine, *Supercond. Sci. Technol.* **29**, 025006 (2016).
- 32 A. Wiederhold, M. R. Koblischka, K. Inoue, M. Muralidhar, M. Murakami, and U. Hartmann, *J. Phys.: Conf. Ser.* **695**, 012004 (2016).
- 33 G. Blatter, M. V. Feigel’man, V. B. Geshkenbein, A. I. Larkin, and V. M. Vinokur, *Rev. Mod. Phys.* **66**, 1125 (1994).
- 34 B. Dam, J. M. Huijbregtse, F. C. Klaassen, R. C. F. van der Geest, G. Doornbos, J. H. Rector, A. M. Testa, S. Freisem, J. C. Martinez, B. Stauble-Pumpin, and R. Griessen, *Nature* **399**, 439 (1999).
- 35 E. Mezzetti, R. Gerbaldo, G. Ghigo, L. Gozzelino, B. Minetti, C. Camerlingo, A. Monaco, G. Cuttone, and A. Rovelli, *Phys. Rev. B* **60**, 7623 (1999).
- 36 Ö. Polat, J. W. Sinclair, Y. L. Zuev, J. R. Thompson, D. K. Christen, S. W. Cook, D. Kumar, Y. Chen, and V. Selvamanickam, *Phys. Rev. B* **84**, 024519 (2011).
- 37 N. Haberkorn, M. Miura, J. Baca, B. Maiorov, I. Usov, P. Dowden, S. R. Foltyn, T. G. Holesinger, J. O. Willis, K. R. Marken, T. Izumi, Y. Shiohara, and L. Civale, *Phys. Rev. B* **85**, 174504 (2012).
- 38 M. R. Koblischka and R. J. Wijngaarden, *Supercond. Sci. Technol.* **8**, 199 (1995).
- 39 C. Jooss, J. Albrecht, H. Kuhn, S. Leonhardt, and H. Kronmüller, *Rep. Prog. Phys.* **65**, 651 (2002).
- 40 A. Yamamoto, J. Shimoyama, K. Kishio, and T. Matsushita, *Supercond. Sci. Technol.* **20**, 658–666 (2007).

⁴¹Z. X. Shi, M. Tokunaga, T. Tamegai, Y. Takano, K. Togano, H. Kito, and H. Ihara, *Phys. Rev. B* **68**, 104513 (2003).

⁴²M. Eisterer, *Phys. Rev. B* **77**, 144524 (2008).

⁴³G. Fuchs, W. Häfner, K. Nenkov, J. Scheiter, O. Perner, A. Handstein, T. Kanai, L. Schultz, and B. Holzapfel, *Supercond. Sci. Technol.* **26**, 122002 (2012).

⁴⁴K. Berger, M. R. Koblischka, B. Douine, J. Noudem, P. Bernstein, T. Hauet, and J. Lévêque, *IEEE Trans. Appl. Supercond.* **26**, 6801005 (2016).

⁴⁵T. Miyazaki, S. Fukui, J. Ogawa, T. Sato, T. Oka, J. Scheiter, W. Häfner, E. Kulawansa, Z. Yuanding, and K. Yokoyama, *IEEE Trans. Appl. Supercond.* **27**, 6800504 (2017).